ACS APPLIED MATERIALS & INTERFACES

Research Article

www.acsami.org

Flexible Photodiodes Based on Nitride Core/Shell p−n Junction Nanowires

Hezhi Zhang,[†] Xing Dai,[†] Nan Guan,[†] Agnes Messanvi,[†,‡,§] Vladimir Neplokh,[†] Valerio Piazza,[†] Martin Vallo,[§] Catherine Bougerol,[‡,§] François H. Julien,[†] Andrey Babichev,[†,⊥] Nicolas Cavassilas,[#] Marc Bescond,[#] Fabienne Michelini,[#] Martin Foldyna,[▽] Eric Gautier,[‡,^] Christophe Durand,[‡,§] Joël Eymery,[§] and Maria Tchernycheva*[,†]

[†]Centre de Nanosciences et de Nanotechnologies, UMR9001 CNRS, University Paris Sud, University Paris Saclay, Orsay 91405, France

[‡]Université Grenoble Alpes, Grenoble 38000, France

[§]"Nanophysique et Semiconducteurs" group, CEA, INAC-SP2M, 17 rue des Martyrs, Grenoble 38000, France

[∥]"Nanophysique et Semiconducteurs" group, CNRS, Institut Néel, 25 rue des Martyrs, Grenoble 38000, France

[⊥]ITMO University, St. Petersburg 197101, Russia

[#]Aix Marseille Université, CNRS, Université de Toulon, IM2NP UMR 7334, 13397 Marseille, France

[▽]LPICM-CNRS, Laboratoire de Physique des Interfaces et Couches Minces, Ecole Polytechnique, Palaiseau 91128, France

[^]CEA, INAC-SPINTEC, 38000 Grenoble, France

ABSTRACT: A flexible nitride p-n photodiode is demonstrated. The device consists of a composite nanowire/polymer membrane transferred onto a flexible substrate. The active element for light sensing is a vertical array of core/shell p−n junction nanowires containing InGaN/GaN quantum wells grown by MOVPE. Electron/hole generation and transport in core/shell nanowires are modeled within nonequilibrium Green function formalism showing a good agreement with experimental results. Fully flexible transparent contacts based on a silver nanowire network are used for device fabrication, which allows bending the detector to a few millimeter curvature radius without damage. The detector shows a photoresponse at wavelengths shorter than 430 nm with a peak responsivity of 0.096 A/W at 370 nm under zero bias. The operation speed for a 0.3 × 0.3 cm^2 detector patch was tested between 4 Hz and 2 kHz. The −3 dB cutoff was found to be ∼35 Hz, which is faster than the operation speed for typical photoconductive detectors and which is compatible with UV monitoring applications.

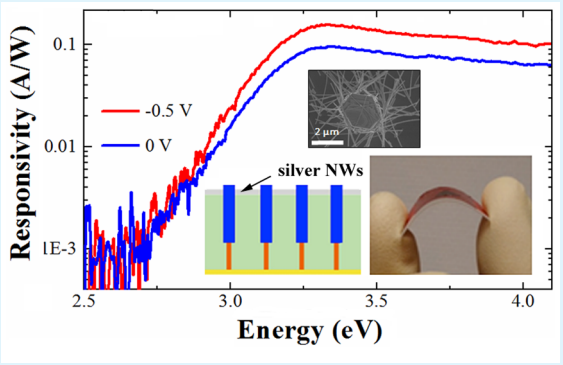

KEYWORDS: *flexible photodiode, nitride nanowires, InGaN, core/shell p−n junction, self-powered photodetectors*

INTRODUCTION

The ultraviolet A (UVA) spectral region (320−400 nm) is a major component of the UV solar radiation, which corresponds to more than 99% of UV light that reaches the earth surface. At high dose, UVA sunlight generates a severe oxidative stress in cells and is harmful for human health; however, moderate exposure to UVA can be favorable, in particular stimulating the vitamin D generation.[1] In this context, the development of wearable UV sensors helping people to balance their sun exposure is today an important societal challenge.[2] In addition to high sensitivity and spectral selectivity, wearable UV sensors need to be lightweight and flexible in order to be easily incorporated in skin patches or integrated on clothes. Autonomous operation without external bias is also an important requirement for this application. Today, there exist a large number of commercially available UV sensors;[3] however, they remain rather bulky and cannot be integrated directly on human clothes or skin.[4] Today, nanomaterials are extensively investigated for UV sensing as a way to enable high sensitivity combined with a possible integration on fabric and self-powering.[5,6]

Wide bandgap nanowire (NW) photodetectors can successfully respond to the above-mentioned specifications for a wearable UV sensor. NW photoconductors based on nitride or oxide materials were reported to exhibit a very high sensitivity thanks to the separation of photogenerated carriers in radial direction.[7−11] NW arrays are also reported to enhance the light absorption by light trapping[12] and antireflection[13] effects, which

Received: May 29, 2016
Accepted: September 12, 2016
Published: September 12, 2016

DOI: 10.1021/acsami.6b06414
ACS Appl. Mater. Interfaces 2016, 8, 26198−26206

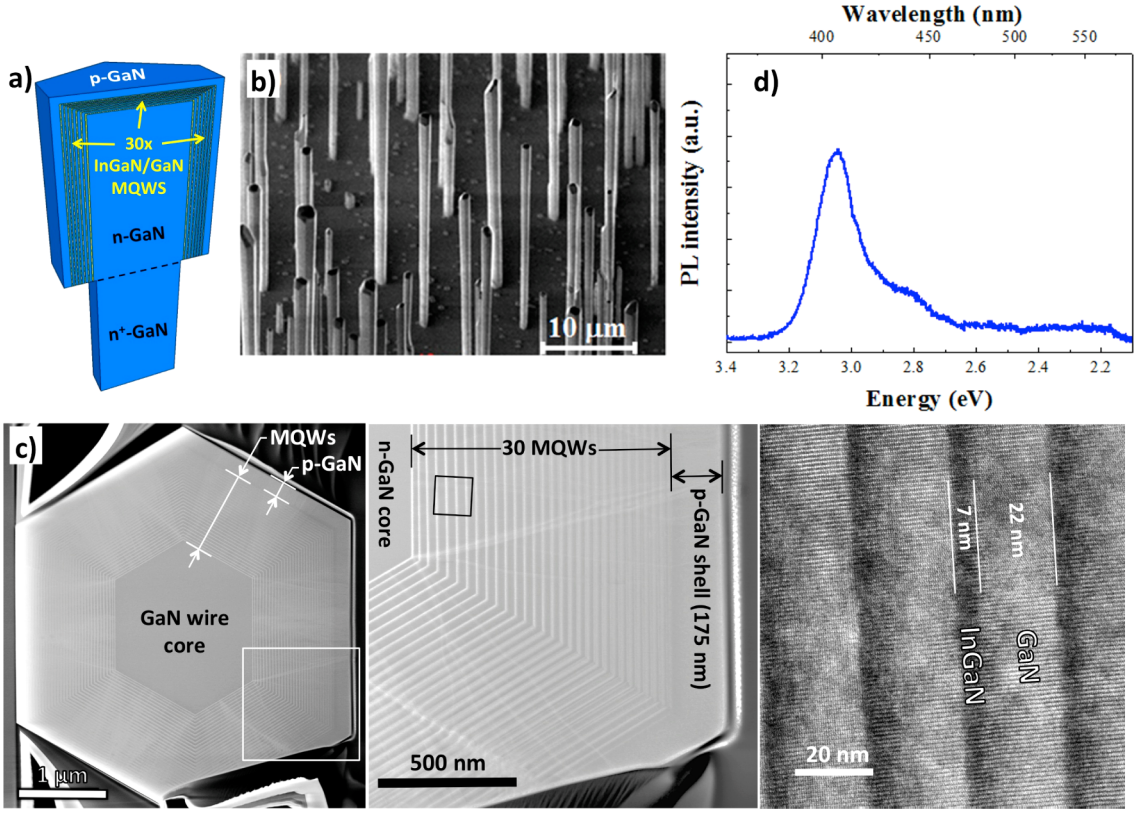

Figure 1. (a) Schematic of the core−shell MQW NW structure. (b) SEM image of the NW array. (c) Transversal cross-sectional STEM-HAADF images taken along the c-zone axis evidencing the core−shell structure on m-plane hexagonal facets (wire slice prepared by FIB technique). The increasing magnification of TEM images reveals that the shell is composed of 30 × InGaN (7 nm)/GaN (22 nm) MQWs coated with a thick p-GaN layer. (d) μPL of a single NW measured at 4 K.

can lead to a high sensitivity even for a small amount of active material. The use of wide bandgap semiconductors naturally provides spectral selectivity by the bandgap absorption cutoff without the use of additional optical filters. In particular, ternary InGaN alloys can be employed to precisely tune the absorption cutoff to the desired wavelength (for example, in order to adjust the detection to wavelengths of UVA shorter than 400 nm).[14,15] Finally, thanks to their small diameter, NWs can stand large deformations without damage.[16,17] This last property enables their use as an active material for flexible optoelectronic devices.[18,19]

Many realizations of flexible UV detectors have been reported, mainly based on ZnO photoconductors.[20,21] However, photoconductors, despite many efforts,[13] still suffer from long response time constants.[22] The operation speed can be significantly enhanced by changing the operation principle from a photoconductor to a photodiode.[15] In addition, p-n photodiodes can operate under zero bias without any need for external polarization, which is a major advantage for their application as portable UV sensors.

The flexible detector fabrication typically follows one of the two approaches: direct NW growth on plastic substrates[13,20,23] or NW transfer to plastic by different methods such as electrospinning method,[24] printing,[21,25] dielectrophoretic positioning,[26] etc. The direct growth on plastic severely restricts the choice of the growth techniques (by limiting the growth temperature) and as a consequence the NW materials that can be synthesized. Transfer methods are potentially applicable to any NW material. However, for the majority of transfer methods, the NWs are positioned horizontally on the substrate, which eliminates the benefit of absorption enhancement in a NW ensemble due to light trapping. The initial NW orientation cannot be maintained. Recently, an alternative transfer method yielding vertical NWs has gained a broad interest.[18,19,27,28] It is based on NW embedding in a polymer layer followed by either mechanical peeling of the membrane,[18,27] or under-etching of a sacrificial layer.[19,28] Following this method, a flexible Schottky photodiode based on CVD-grown GaN NWs has been demonstrated.[29] Unfortunately, deep defects in CVD-grown GaN wires yield a strong photoresponse in the visible spectral range, which does not allow for selective detection of UVA. It is desirable to replace the defect-related absorption by the above-bandgap absorption, which can be better controlled in particular by using ternary alloys for tuning the absorption edge. This is the objective of the present study.

In this work we demonstrate for the first time a flexible nitride p-n photodiode. The device employs core/shell p−n junction NWs grown by metalorganic vapor phase epitaxy (MOVPE) on sapphire substrates. InGaN/GaN quantum wells (QWs) are inserted in the active region to extend the detection range to wavelengths longer than the GaN near band edge cutoff. We employ a mechanical peeling transfer method,[18] which allows to maintain the NW orientation. This is of particular importance for the p-n NWs, for which the polarity of the junction should be preserved for all wires contacted in parallel. The NWs were embedded into a polymer layer and the polymer/NW membrane was mechanically peeled-off, contacted and mounted on a piece of a copper tape. A fully flexible transparent contact based on a silver nanowire network was used, which allows bending the detector to a few millimeters

DOI: 10.1021/acsami.6b06414
ACS Appl. Mater. Interfaces 2016, 8, 26198−26206

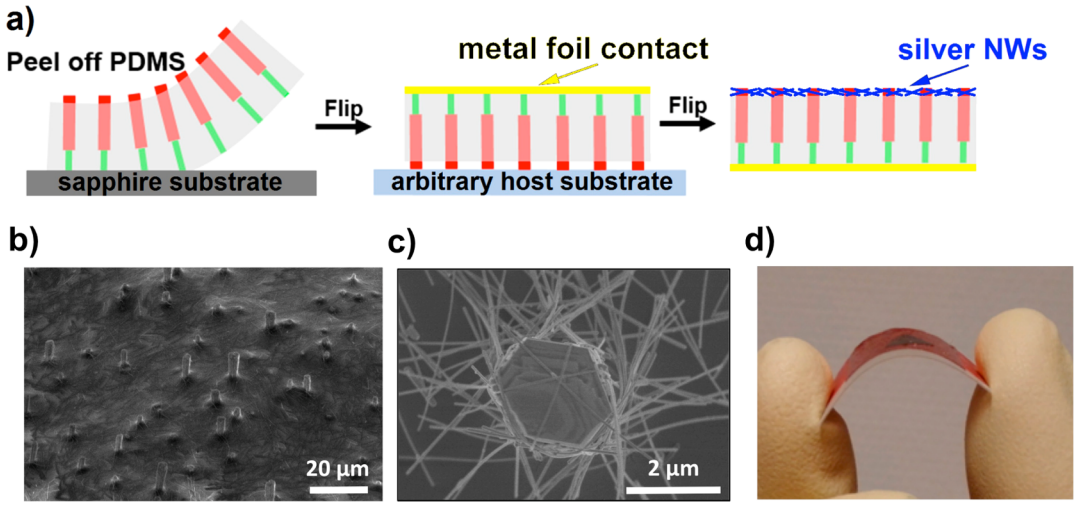

Figure 2. (a) Schematic representation of the fabrication steps: encapsulation in PDMS and peel-off of the membrane; deposition of the back metal contact; deposition of the top transparent contact composed of a silver nanowire mesh. (b) Bird's eye view SEM image of the top surface of the detector. (c) Top view SEM image of an individual nitride NW contacted with silver nanowires. (d) Device photo illustrating its flexibility.

curvature radius without damage. Without any external bias, the detector shows a photoresponse at wavelengths shorter than 430 nm with a peak responsivity of 0.096 A/W at 370 nm. The operation speed of a 0.3 × 0.3 cm^2 detector patch was tested between 4 Hz and 2 kHz. The −3 dB cutoff was found to be ∼35 Hz, which is faster than the operation speed for typical photoconductive detectors and which is compatible with UV monitoring applications. Angular dependence of the photoresponse was analyzed.

EXPERIMENTAL SECTION

Nanowire Growth. The core−shell NWs containing GaN/InGaN multiple quantum wells (MQWs) were grown on c-sapphire substrates. An MOVPE growth method has been employed using a closed coupled showerhead reactor. The approach to grow the self-assembled c-GaN wires on sapphire is based on an in situ thin SiN layer deposition acting as a partial mask. The vertical growth was favored by using a high flux of silane (200 nmol/min), a low V/III ratio (50), a high temperature (1040 °C), and a high pressure (800 mbar) as described in detail in ref 30. A first section of about 5 μm is grown with silane injection under trimethylgallium (TMGa) precursor and ammonia (NH_3) flux leading to a spontaneous SiN_x passivation of the wire sidewalls that maintains the wire geometry[31,32] and to a high n^+-type doping of the wire core (donor concentration around ∼10^{20} cm^{-3} [33]). By stopping the silane flux, a second nonintentionally doped section (10^{18} cm^{-3} [34]) is grown to reach a length of about 25 μm. Thirty radial InGaN/GaN QWs are subsequently grown around the top unpassivated wire section corresponding to the nonintentionally doped part at 400 mbar under the injection of triethylgallium (TEGa), trimethylindium (TMIn), and ammonia at 720 °C for the InGaN wells (In-content target about 18%) and 900 °C for the GaN barriers. The nominal thickness is 3 and 10 nm for the wells and barriers, respectively. A final p-GaN thick shell of about 150 nm is grown at 920 °C with a biscyclopentadienyl-magnesium precursor (Cp_2Mg) followed by a dopant activation annealing performed at 750 °C for 20 min in N_2 atmosphere (acceptor concentration around ∼10^{16}−$10^{17}$$cm^{-3}$ [34]).

The schematic of Figure 1a illustrates the core/shell NW internal structure, while Figure 1b presents an SEM image of an as-grown NW array illustrating the wire morphology. The average wire height is 25 ± 5 μm, and the diameter is around 1−2 μm. The typical wire density is about 10^6 cm^{-2}. We note that this growth procedure yields MQWs not only on the m-plane lateral sidewalls, but also on the top c plane, with a different QW thickness and In content.[35]

The internal wire structure was probed by scanning transmission electron microscopy (STEM) in high-angle annular dark-field (HAADF) imaging mode. A thin slice perpendicular to the wire axis was prepared by focused ion beam (FIB) in order to observe the wire cross-section in transversal direction. Figure 1c shows STEM-HAADF images at three increasing magnifications taken along the *c*-zone axis on the same wire transversal slice. A clear core−shell structure is observed around wire sidewalls corresponding to m-planes facets evidencing the presence of 30 InGaN/GaN MQWs followed by a p-type GaN shell. The thickness of InGaN wells in dark contract is estimated to be 7 ± 1 nm while the GaN barriers are 22 ± 2 nm. The thickness of the p-GaN surrounding shell is measured to be ∼175 nm. We observe that the external interface of the wells (corresponding to the InGaN/GaN interface) is significantly rougher compared to the internal well interface (corresponding to the GaN/InGaN interface), as generally observed for InGaN/GaN heterostructures, especially with thick wells. The In-content in the well has been estimated close to 15%[36] instead of the targeted 18% due to lower incorporation of In on the m-plane surfaces.[37] In Figure 1c, we observe that the MQW structure can be disturbed by dislocations and stacking faults originating from the first QW interface that propagate across the whole shell heterostructure. These morphological properties of the core−shell structure are consistent with the previously reported core−shell structures grown under similar growth conditions for photovoltaic applications.[38]

The optical properties of NWs were investigated by low temperature microphotoluminescence (μPL) spectroscopy. In order to avoid excitation of multiple NWs, the NWs were cut from their substrate by an ultrasonic bath and dispersed with a low density on a Si substrate. The μPL characterization was carried out at 4 K by exciting single NWs at 375 nm wavelength by a continuous wave laser diode. The luminescence signal was collected by a HR460 spectrometer and a charge coupled device (CCD) camera. Figure 1 b) shows a typical μPL spectrum of a single NW. The spectrum presents two contributions. The main peak at 3.07 eV (403 nm) is attributed to the radial QWs on the m-plane. A weak shoulder peak observed at a lower energy around 2.8 eV (442 nm) originates from the axial QWs at the top part of the NW as previously reported in ref 35.

Flexible Photodetector Fabrication. The fabrication of flexible photodetectors started by forming an ohmic contact to the p-GaN shell. A photoresist layer was spin-coated on the as-grown NWs to protect the highly n-doped GaN base of the NWs. Then a semitransparent 3 nm/3 nm Ni/Au metallic layer was deposited by e-beam evaporation on the p-GaN shells protruding from the resist. The metal was lifted-off and the sample was annealed at 400 °C in air for 10 min. The presence of this thin Ni/Au layer allows an ohmic

DOI: 10.1021/acsami.6b06414
ACS Appl. Mater. Interfaces 2016, 8, 26198−26206

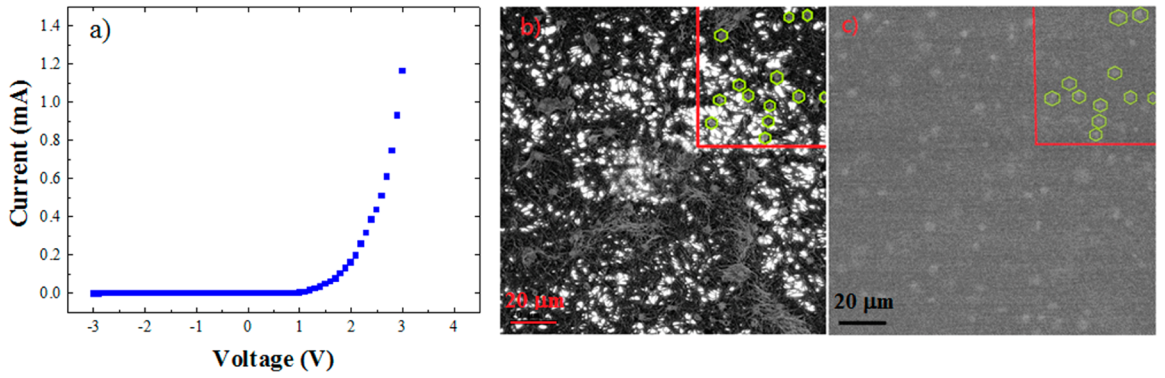

Figure 3. (a) I–V curve of the flexible photodetector. (b) Top-view SEM image of the detector contacted with silver nanowires and (c) the corresponding EBIC map (bright contrast corresponds to the induced current in nitride NWs).

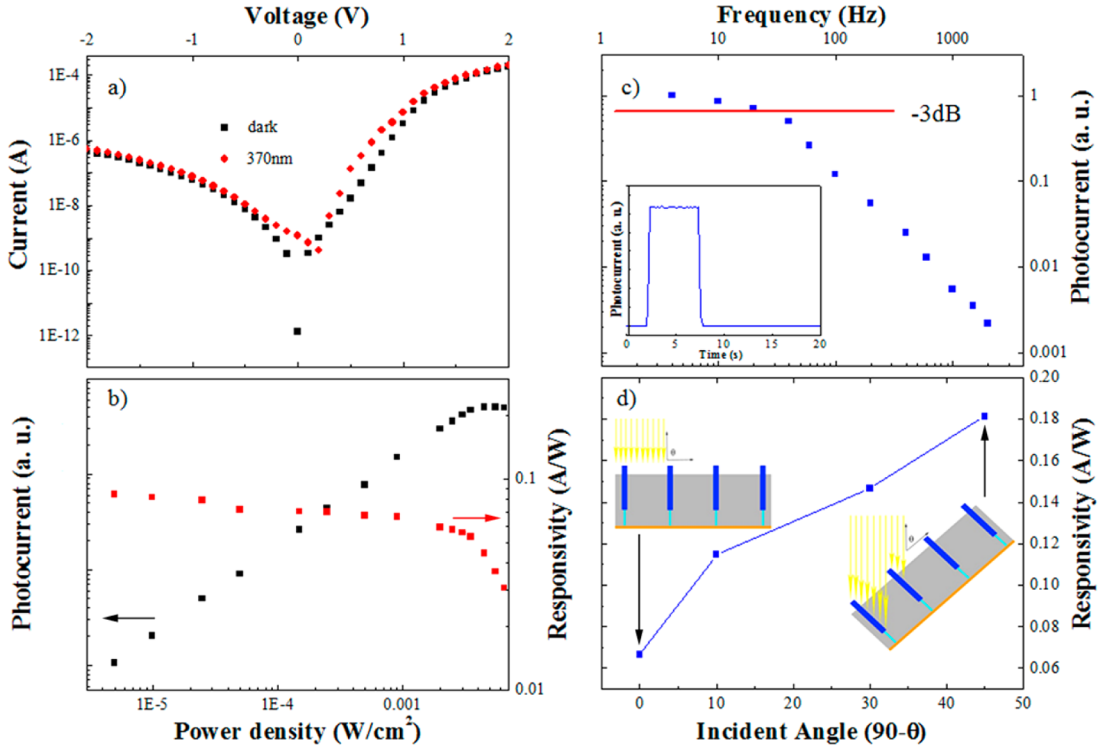

Figure 4. (a) I–V curve in the dark and under illumination with λ = 370 nm. (b) Power dependence of the responsivity. (c) Frequency response of the detector. Inset shows the current trace under zero bias in response to a square light pulse. (d) Angular dependence of the responsivity at different angles from θ = 0° to 45°. Insets show schematics explaining the illumination configuration under normal and oblique incidence.

contact to form to the p-GaN shells. The NWs were then encapsulated into polydimethylsiloxane polymer (PDMS) with an average thickness of 25 μm. The composite nanowire/PDMS membrane was peeled-off from the sapphire substrate and flipped upside down to metalize the bottom part of the NWs. An ohmic Ti/Al/Ti/Au (10 nm/30 nm/10 nm/200 nm) contact was deposited on the NW highly n-doped bases. Then the device was again flipped upside-down and transferred to a flexible substrate (copper tape). The transparent top contact was deposited by spin-coating on the surface using a suspension of silver nanowires to achieve a flexible network connecting the p-GaN shells. The contact area is approximately 0.3 × 0.3 cm^2. The fabrication process is schematically illustrated in Figure 2a. The SEM image (Figure 2b) shows a bird's eye view of the device. The distribution of silver nanowires is uniform. The GaN NWs are well connected by silver nanowires as illustrated in a close-up SEM image of Figure 2c. The density of protruding GaN NWs connected by the silver nanowires is ~1.2 × 10^6 cm^{-2}. Figure 2d presents a photo of the device and illustrates its flexibility.

We note that the main challenge in the fabrication process is the realization of a flexible transparent ohmic contact. For the bottom opaque contact, a standard metallization is used, which provides an ohmic contact to the n-GaN NW bases. Metal contacts were shown to well sustain bending deformations for curvature radiuses of several millimeters.[39−43] Therefore, they are commonly used for flexible LEDs and photodetectors.[44,45] However, standard metal contacts are opaque and do not allow for light coupling into the NW photodiode. Following our previous developments, we have chosen a silver nanowire mesh as a top transparent contact.[18] This type of contacts is today intensively studied in the literature as an alternative to ITO, which combines mechanical flexibility with optical transparency and low resistance.[46,47]

Flexible Photodetector Characterization Techniques. The electrical characteristics of the flexible photodetector were investigated using a Janis probe station and a Keithley 2636 source-meter at room temperature. The spectral dependence of the photocurrent was analyzed by illuminating the device with a wavelength tunable xenon lamp light coupled with a Jobin Yvon Triax 180 spectrometer. A

DOI: 10.1021/acsami.6b06414
ACS Appl. Mater. Interfaces 2016, 8, 26198−26206

calibrated photodiode sensor was used to measure the light source output intensity, which was then used to normalize the photocurrent spectra. The photo responsivity of the detector was calibrated using a continuous wave laser diode emitting at 375 nm wavelength. In addition, electron beam induced current (EBIC) measurements were performed to probe the top contact properties. EBIC maps were collected at room temperature using an acceleration voltage of 20 kV in a Hitachi SU8000 SEM controlled by Gatan Digiscan system as described in ref 48.

RESULTS AND DISCUSSION

Electrical Characterizations. A current−voltage (I−V) curve in the dark of the fabricated flexible photodetector is displayed in Figure 3a. The curve exhibits a typical rectifying behavior with a diode knee voltage around 2.3 V, after which the forward current increases steeply. Under reversed bias, the leakage current is negligible up to −3 V. The diode-like I−V characteristic validates the fabrication procedure, showing that the PDMS membrane provides a good electrical insulation and that there is no pronounced Schottky contact between the p-GaN shell and the silver nanowire contact, which would otherwise block the forward current. The I−V measurements were repeated after 50 cycles of device bending down to a radius of 5 mm. No modification of the I−V curve was observed.

To probe the electrical connection between the silver nanowires and the nitride NWs and to evaluate the long-range conductivity of the silver nanowire top contact, EBIC mapping was performed on the flexible photodetector. Figure 3b,c presents the SEM image and the EBIC map (under zero bias) of the top surface of the detector. The electron beam arriving at the sample surface creates electron−hole pairs in the core/shell nitride NWs, which are separated by the internal electrical field of the p−n junction and then collected by the electrodes.[48] The induced current appears as a bright contrast in Figure 3c. The region probed by EBIC in Figure 3 is located 1 mm away from the metal bonding pad, and there is no current spreading grid on top of the silver nanowire network. No significant attenuation of the EBIC signal with distance from the bonding pad is observed, which proves that the carrier transport by the silver nanowires network is efficient. By comparing the SEM and the EBIC maps, we evaluated the number of nitride NWs protruding from PDMS (and thus contacted by silver nanowires) and the number of NWs generating EBIC signal. As an example, the positions of the NWs are highlighted with green hexagons in the upper right part of the maps. The number of NWs generating EBIC signal corresponds to 85% of all protruding NWs. This value gives an estimation of the yield offered by the present silver nanowire contacting technique.

Electro-optical Characterizations. The inset of Figure 4a shows the I−V curves of the detector in the dark and under illumination with UV light (λ = 370 nm, 1.26 × 10^{-8} W power) in logarithmic scale. Under zero bias, the photocurrent is negative, the corresponding responsivity is ∼0.1 A/W. Under forward bias, the photocurrent changes sign at ∼0.25 V. This relatively low value may be related to some defects in the active region.

The power dependence of the responsivity has been probed by illuminating the detector with an Ar^{2+} ion laser (λ = 244 nm) and varying the incident power density by almost 4 orders of magnitude (from 5 × 10^{-6} to 7 × 10^{-3} W/cm^2). As shown in Figure 4b, at moderate excitation power densities (up to ∼3 × 10^{-3} W/cm^2), the photocurrent presents almost a linear dependence with power. The responsivity slightly decreases from 0.084 to 0.057 A/W in this region. At high power densities the photocurrent dependence becomes sublinear and the photocurrent saturates. Correspondingly, the responsivity decreases down to 0.03 A/W at 7 × 10^{-3} W/cm^2. Similar power dependence has been reported in axial junction NW photodiodes.[49] In thin film p−n photodiodes the response is linear up to higher power densities (0.2 W/cm^2 [50]). The saturation at high excitation is related to the screening of the built-in field by the photogenerated carriers.

The detector operation speed was analyzed. First, the detector response to a square light pulse (λ = 370 nm) was measured under zero bias. The inset of Figure 4c shows the temporal current trace. The flexible photodetector presents a fast response with a rise and decay switching time below 0.1 s (which is the time resolution of our measurement system). To further investigate the device operation speed, the frequency dependence of the photocurrent was measured at zero bias using a mechanically chopped illumination and a lock-in detection. Figure 4c shows the detector frequency response from 4 to 2000 Hz. The −3 dB cutoff frequency of the large area (0.3 × 0.3 cm^2) device is ∼35 Hz. This operation speed is higher than the typical values for NW photoconductors[8,11] and is comparable to the one of the axial p-i-n NW photodiodes.[49] We note that it is compatible with the potential application of UV monitoring.

The angular dependence of the photodetector responsivity was investigated. The photocurrent was collected under zero bias for incident angles θ between 0 and 45 deg for a power density of 0.001 W/cm^2 (i.e., in the range where the photocurrent shows an almost linear dependence on the incident power as shown in Figure 4b). As reported in Figure 4d, the responsivity increases with the incident angle. The responsivity is ∼0.066 A/W for the laser light perpendicular to the sample surface, whereas it increases to 0.18 A/W for a 45 deg tilt. This phenomenon can be explained by the enhanced light harvesting when the sample is rotated. Indeed, the density of nitride NWs obtained by self-catalyzed MOVPE growth is low, they cover only ∼3.8% of the total detector surface. At normal incidence, only a small part of the NW surface (mainly their top surface) absorbs light, as illustrated in the inset of Figure 4d. The effects of light concentration reported for nanowire solar cells[51] do not play important role for the wire diameters in the 1−2 μm range that are used in this study. When the photodetector is tilted, the light is absorbed not only by the top surface but also by the NW side walls, which increases the portion of the absorbed light and induces a stronger photocurrent for the same power density.

The spectral response of the detector was analyzed. Figure 5 displays the room temperature photocurrent spectra in logarithmic scale under zero bias and under reverse bias of −0.5 V, respectively. The low-energy onset of the photocurrent (i.e., the energy value, for which the photocurrent clearly dominates over the noise) is around 2.88 eV (430 nm). At higher energies, the photocurrent increases by more than 1 order of magnitude, reaching its maximum at 3.35 eV (370 nm) and then slightly decreasing. The bandgap of the radial QWs is estimated to be close to 3.03 eV (410 nm) at room temperature (according to μPL measurements discussed above and accounting for the Varshni shift with temperature). Therefore, the low-energy onset value of the photocurrent is below the bandgap of the radial QWs. This is most likely due to the contribution to the photocurrent of the axial QWs, which have

DOI: 10.1021/acsami.6b06414
ACS Appl. Mater. Interfaces 2016, 8, 26198−26206

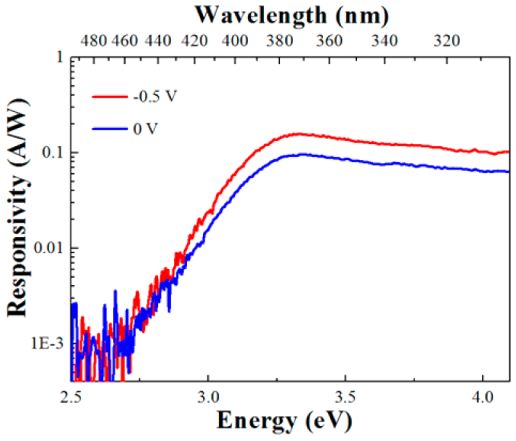

Figure 5. Room temperature photocurrent spectrum in logarithmic scale under zero bias and under reverse −0.5 V, respectively.

a smaller bandgap value due to both their higher In concentration and to the quantum confined Stark effect induced by the internal electric field along the *c*-axis. Nevertheless, the overall spectral response matches quite well the UVA spectral domain, which validates the possible application of the developed photodiode for UVA sensing.

The peak responsivity of the detector reaches its maximum value of 0.096 A/W at 3.35 eV. We note that the density of the active NWs is quite low in the present device; a higher value can be reached with a higher density NW array. A decrease of the photocurrent for energies above 3.4 eV is observed (the responsivity drops to 0.063 A/W at 4.1 eV). This decrease is typical also for thin film nitride photodiodes and can be attributed to the high absorption coefficient of GaN above the bandgap, which makes the absorption depth small. The carriers are generated close to the surface of the p-doped GaN layer and have a large probability to recombine on surface states before being collected. The same explanation can be applied in the present case for the enhanced light absorption close to the top NW surface. Under a reverse bias of −0.5 V, the spectral shape remains similar whereas the photocurrent signal increases. The peak responsivity becomes 0.157 A/W. In agreement with theoretical modeling presented in the next section, this signal enhancement is attributed to the increase of the electric field in the active region facilitating the carrier extraction from the QWs. For energies above the GaN bandgap the signal increase under reverse bias can also be due to a slight broadening of the space-charge region in the p−n junction.

Modeling of Current Generation in the Active Region. The photocurrent generation in the InGaN/GaN p−n junction QWs has been modeled using the nonequilibrium Green

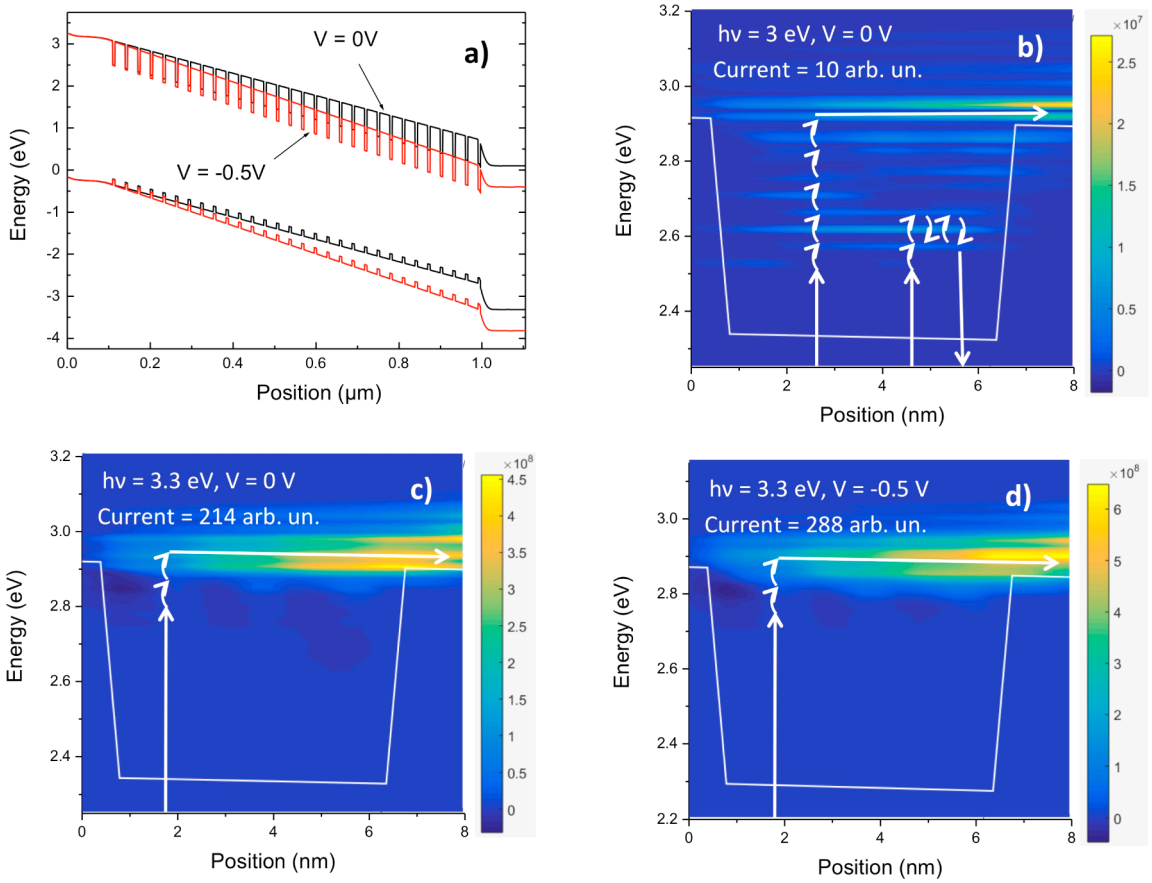

Figure 6. (a) Conduction band and valence band potential profiles in the entire active region for external biases of 0 V and −0.5 V. Photocurrent spectra in conduction band versus position in a representative QW under illumination for (b) V = 0 V, illumination at 3 eV; (c) V = 0 V, illumination at 3.3 eV, and (d) V = −0.5 V, illumination at 3.3 eV. For the current the color legend is in Arb. Unit. In panels (b−d) arrows schematically represente physical phenomena involved in the extraction of carriers. The vertical arrows represent the interband interactions (photon absorption/emission). The curved arrows represent the intraband interactions (phonon absorption/emission). The horizontal arrows represent the diffusion process.

DOI: 10.1021/acsami.6b06414
ACS Appl. Mater. Interfaces 2016, 8, 26198−26206

function formalism. This model is described in details in ref.[52] This approach considers the quantum character of electrons, which cannot be neglected in the present device with an active region containing QWs, since in QWs the confinement and the tunneling both control the electronic transport. Moreover, as we show, the electron−phonon scattering has also a key role in the photodetector operation.

The first step of the calculations is the determination of the potential profile in the entire active region in the dark. Figure 6a displays the conduction band and valence band profiles for 30 InGaN/GaN MQWs with a nominal composition of 18%. The calculations are performed for zero external bias and for −0.5 V reverse bias. Zero of energy corresponds to the Fermi level in the p-GaN layer. The built-in field of the p−n junction is distributed homogeneously over the 29 left QWs which are empty in the dark. Only the first QW next to the n-GaN layer is filled with electrons. The electron density in this well is 10^{18} and 1.3×10^{18} cm^{-3} at −0.5 and 0 V, respectively.

Due to the computational burden of the method, the photocurrent is only calculated for one representative QW. The procedure is described in ref 53. To illustrate the evolution of the photocurrent with the photon energy, Figure 6b,c presents the current maps as a function of position and energy in the conduction band of a QW in an unbiased p−n junction under illumination with 3 eV (i.e., deep in the InGaN QW) and with 3.3 eV (i.e., slightly below the barrier bandgap), respectively. The calculation predicts that the responsivity increases by a factor of 21 when the photon energy increases. This prediction is in qualitative agreement with the experimental results shown above, for which the photocurrent signal increases ∼9 times between 3 and 3.3 eV (cf. Figure 5). As shown by the quantification of the spectrum presented in Figure 6a, when electrons are generated deep in the well, the scattering with phonons controls the extraction (the optical phonon energy is 92 meV). The interaction with phonons is schematically illustrated with curved arrows in Figure 6b−d. In this case, a large number of phonon-absorption is necessary to extract the photogenerated carriers from the QW. This current is then expected to increase with temperature. In contrast, as shown in Figure 6c for excitation with a photon energy of 3.3 eV, the electrons can be withdrawn from the well without a large number of phonon scatterings. The electronic extraction is then easier and the current is larger.

To simulate the photodetector response under bias, the photocurrent for a reverse bias of −0.5 V has been calculated. Figure 6a shows the increase of the electric field in the whole active region with the reverse bias. The corresponding current spectrum for the incident photon energy of 3.3 eV is shown in Figure 6d. The model predicts the current increase by a factor of 1.34 under bias, which is in qualitative agreement with the experimental value of 1.61 (cf. Figure 5)). By comparing the spectra presented in Figure 6c,d, it is clear that the reverse bias facilitates the direct extraction of photogenerated carrier without any scattering with phonons. However, the tunneling is not observed since the barriers are too thick.

CONCLUSIONS

In conclusion, a flexible nitride p−n photodiode has been demonstrated using core/shell p−n junction NWs containing InGaN/GaN QWs. The polymer membranes embedding active nitride NWs were contacted using a transparent silver nanowire mesh to ensure high mechanical flexibility. Without any external bias, the detector shows a photoresponse at wavelengths shorter than 430 nm with a peak responsivity of 0.096 A/W at 370 nm. The −3 dB cutoff frequency for a 0.3 × 0.3 cm^2 detector patch was found to be ∼35 Hz, which is compatible with UV monitoring applications. The detector photoresponse increases for an oblique incidence angle due to an increased light absorption.

AUTHOR INFORMATION

Corresponding Author

*Tel.: +33 1 69 15 40 51. E-mail: maria.tchernycheva@u-psud.fr.

Notes

The authors declare no competing financial interest.

ACKNOWLEDGMENTS

This work has been partially financially supported by ANR "Investissement d'Avenir" programs "GaNeX" (ANR-11-LABX-2014) and "NanoSaclay" (ANR-10-LABX-0035), by ANR-14-CE26-0020-01 project "PLATOFIL", and by EU ERC project "NanoHarvest" (Grant No. 639052). A.B. acknowledges the support of RFBR (Project Nos. 15-02-08282 and 16-29-03289), and program of fundamental research of the Presidium of the RAS No. 1 (Project No. 1.3.3.3). The device processing has been performed at CTU-IEF-Minerve technological platform, member of the Renatech RTB network.

REFERENCES

(1) Holick, M. F. Sunlight and Vitamin D for Bone Health and Prevention of Autoimmune Diseases, Cancers, and Cardiovascular Disease. *Am. J. Clin. Nutr.* **2004**, *80* (6), 1678S−1688S.

(2) Zhang, X.; Xu, W.; Huang, M. C.; Amini, N.; Ren, F. *See UV on Your Skin: an Ultraviolet Sensing and Visualization System*. In *Proceedings of the 8th International Conference on Body Area Networks*, Boston, Sept 30th − Oct 2, 2013; Suzuki, J., Wang, H., Eds.; ICST, 2013; Pages 22−28. DOI: 10.4108/icst.bodynets.2013.253701.

(3) http://www.solarmeter.com; accessed on July 31, 2016.

(4) Tang, S. L. P. Recent Developments in Flexible Wearable Electronics for Monitoring Applications. *Trans. Inst. Meas. Control* **2007**, *29* (3−4), 283−300.

(5) Chen, H.; Liu, K.; Hu, L.; Al-Ghamdi, A. A.; Fang, X. New Concept Ultraviolet Photodetectors. *Mater. Today* **2015**, *18* (9), 493−502.

(6) Pang, C.; Lee, C.; Suh, K. Y. Recent Advances in Flexible Sensors for Wearable and Implantable Devices. *J. Appl. Polym. Sci.* **2013**, *130* (3), 1429−1441.

(7) Calarco, R.; Marso, M.; Richter, T.; Aykanat, A. I.; Meijers, R.; vd Hart, A.; Stoica, T.; Lüth, H. Size-Dependent Photoconductivity in MBE-Grown GaN-Nanowires. *Nano Lett.* **2005**, *5* (5), 981−984.

(8) Soci, C.; Zhang, A.; Xiang, B.; Dayeh, S. A.; Aplin, D. P. R.; Park, J.; Bao, X. Y.; Lo, Y. H.; Wang, D. ZnO Nanowire UV Photodetectors with High Internal Gain. *Nano Lett.* **2007**, *7* (4), 1003−1009.

(9) Zhang, H.; Babichev, A. V.; Jacopin, G.; Lavenus, P.; Julien, F. H.; Egorov, A. Y.; Zhang, J.; Pauporté, T.; Tchernycheva, M. Characterization and Modeling of a ZnO Nanowire Ultraviolet Photodetector with Graphene Transparent Contact. *J. Appl. Phys.* **2013**, *114* (23), 234505.

(10) Babichev, A. V.; Zhang, H.; Lavenus, P.; Julien, F. H.; Egorov, A. Y.; Lin, Y. T.; Tu, L. W.; Tchernycheva, M. GaN Nanowire Ultraviolet Photodetector with a Graphene Transparent Contact. *Appl. Phys. Lett.* **2013**, *103* (20), 201103.

(11) González-Posada, F.; Songmuang, R.; Den Hertog, M.; Monroy, E. Room-Temperature Photodetection Dynamics of Single GaN Nanowires. *Nano Lett.* **2012**, *12* (1), 172−176.

(12) Garnett, E.; Yang, P. Light Trapping in Silicon Nanowire Solar Cells. *Nano Lett.* **2010**, *10* (3), 1082−1087.

DOI: 10.1021/acsami.6b06414
ACS Appl. Mater. Interfaces 2016, 8, 26198−26206

(13) Zhang, H.; Hu, Y.; Wang, Z.; Fang, Z.; Peng, L. Performance Boosting of Flexible ZnO UV Sensors with Rational Designed Absorbing Antireflection Layer and Humectant Encapsulation. *ACS Appl. Mater. Interfaces* **2016**, *8* (1), 381−389.
(14) Bugallo, A.; Rigutti, L.; Jacopin, G.; Julien, F. H.; Durand, C.; Chen, X. J.; Salomon, D.; Eymery, J.; Tchernycheva, M. Single-Wire Photodetectors Based on InGaN/GaN Radial Quantum Wells in GaN Wires Grown by Catalyst-Free Metal-Organic Vapor Phase Epitaxy. *Appl. Phys. Lett.* **2011**, *98* (23), 3107.
(15) Zhang, H.; Messanvi, A.; Durand, C.; Eymery, J.; Lavenus, P.; Babichev, A.; Julien, F. H.; Tchernycheva, M. InGaN/GaN Core/Shell Nanowires for Visible to Ultraviolet Range Photodetection. *Phys. Status Solidi A* **2016**, *213* (4), 936−940.
(16) Espinosa, H. D.; Bernal, R. A.; Minary-Jolandan, M. A. Review of Mechanical and Electromechanical Properties of Piezoelectric Nanowires. *Adv. Mater.* **2012**, *24* (34), 4656−4675.
(17) Stan, G.; Krylyuk, S.; Davydov, A. V.; Cook, R. F. Bending Manipulation and Measurements of Fracture Strength of Silicon and Oxidized Silicon Nanowires by Atomic Force Microscopy. *J. Mater. Res.* **2012**, *27* (03), 562−570.
(18) Dai, X.; Messanvi, A.; Zhang, H.; Durand, C.; Eymery, J.; Bougerol, C.; Julien, F. H.; Tchernycheva, M. Flexible Light-Emitting Diodes based on Vertical Nitride Nanowires. *Nano Lett.* **2015**, *15* (10), 6958−6964.
(19) Chung, K.; Beak, H.; Tchoe, Y.; Oh, H.; Yoo, H.; Kim, M.; Yi, G. C. Growth and Characterizations of GaN Micro-Rods on Graphene Films for Flexible Light Emitting Diodes. *APL Mater.* **2014**, *2* (9), 092512.
(20) Farhat, O. F.; Halim, M. M.; Abdullah, M. J.; Ali, M. K. M.; Ahmed, N. M.; Allam, N. K. Growth of Vertically Aligned ZnO Nanorods on Teflon as a Novel Substrate for Low-Power Flexible Light Sensors. *Appl. Phys. A: Mater. Sci. Process.* **2015**, *119* (4), 1197−1201.
(21) Liu, X.; Gu, L.; Zhang, Q.; Wu, J.; Long, Y.; Fan, Z. All-printable Band-Edge Modulated ZnO Nanowire Photodetectors with Ultra-High Detectivity. *Nat. Commun.* **2014**, *5*, 4007.
(22) Dai, X.; Tchernycheva, M.; Soci, C.; Compound Semiconductor Nanowire Photodetectors. In *Semiconductors and Semimetals*; Dayeh, S. A., i Morral, A. F., Jagadish, C., Eds.; Semiconductor Nanowires II: Properties and Applications; Academic Press: Burlington, 2016; Vol. *94*, pp 75−107.
(23) Chen, T. P.; Young, S. J.; Chang, S. J.; Hsiao, C. H.; Wu, S. L. Photoelectrical and Low-Frequency Noise Characteristics of ZnO Nanorod Photodetectors Prepared on Flexible Substrate. *IEEE Trans. Electron Devices* **2013**, *60* (1), 229−234.
(24) Zheng, Z.; Gan, L.; Li, H.; Ma, Y.; Bando, Y.; Golberg, D.; Zhai, T. A Fully Transparent and Flexible Ultraviolet-Visible Photodetector Based on Controlled Electrospun ZnO-CdO Heterojunction Nanofiber Arrays. *Adv. Funct. Mater.* **2015**, *25* (37), 5885−5894.
(25) Chen, G.; Liang, B.; Liu, Z.; Yu, G.; Xie, X.; Luo, T.; Xie, Z.; Chen, D.; Zhu, M.-Q.; Shen, G. High Performance Rigid and Flexible Visible-Light Photodetectors based on Aligned X (In, Ga) P Nanowire Arrays. *J. Mater. Chem. C* **2014**, *2* (7), 1270−1277.
(26) Guilera, J.; Fàbrega, C.; Casals, O.; Hernández-Ramírez, F.; Wang, S.; Mathur, S.; Udread, F.; De Luca, A.; Alie, S. Z.; Romano-Rodríguez, A.; Prades, J. D.; Morantea, J. R. Facile Integration of Ordered Nanowires in Functional Devices. *Sens. Actuators, B* **2015**, *221*, 104−112.
(27) Spurgeon, J. M.; Boettcher, S. W.; Kelzenberg, M. D.; Brunschwig, B. S.; Atwater, H. A.; Lewis, N. S. Flexible, Polymer-Supported, Si Wire Array Photoelectrodes. *Adv. Mater.* **2010**, *22* (30), 3277−3281.
(28) Lee, C. H.; Kim, Y. J.; Hong, Y. J.; Jeon, S. R.; Bae, S.; Hong, B. H.; Yi, G. C. Flexible Inorganic Nanostructure Light-Emitting Diodes Fabricated on Graphene Films. *Adv. Mater.* **2011**, *23* (40), 4614−4619.
(29) Shi, X.; Peng, M.; Kou, J.; Liu, C.; Wang, R.; Liu, Y.; Zhai, J. A Flexible GaN Nanowire Array-Based Schottky Type Visible Light Sensor with Strain-Enhanced Photoresponsivity. *Adv. Electron. Mater.* **2015**, *1* (12), 1500169−1500175.
(30) Koester, R.; Hwang, J. S.; Durand, C.; Dang, D. L. S.; Eymery, J. Self-Assembled Growth of Catalyst-Free GaN Wires by Metal − Organic Vapour Phase Epitaxy. *Nanotechnology* **2010**, *21*, 015602.
(31) Eymery, J.; Salomon, D.; Chen, X. J.; Durand, C. Process for Catalyst-Free Selective Growth on a Semiconductor Structure. Patent WO/2012/136665, April 03 2012.
(32) Tessarek, C.; Heilmann, M.; Butzen, E.; Haab, A.; Hardtdegen, H.; Dieker, C.; Spiecker, E.; Christiansen, S. The Role of Si during the Growth of GaN Micro- and Nanorods. *Cryst. Growth Des.* **2014**, *14*, 1486−1492.
(33) Tchoulfian, P.; Donatini, F.; Levy, F.; Amstatt, B.; Dussaigne, a.; Ferret, P.; Bustarret, E.; Pernot, J. Thermoelectric and Micro-Raman Measurements of Carrier Density and Mobility in Heavily Si-Doped GaN Wires. *Appl. Phys. Lett.* **2013**, *103*, 202101.
(34) Tchoulfian, P.; Donatini, F.; Levy, F.; Dussaigne, A.; Ferret, P.; Pernot, J. Direct Imaging of P-N Junction in Core-Shell GaN Wires. *Nano Lett.* **2014**, *14*, 3491−3498.
(35) Jacopin, G.; Bugallo, A. D. L.; Lavenus, P.; Rigutti, L.; Julien, F. H.; Zagonel, L. F.; Kociak, M.; Durand, C.; Salomon, D.; Chen, X. J.; Eymery, J.; Tchernycheva, M. Single-Wire Light-Emitting Diodes Based on GaN Wires Containing Both Polar and Nonpolar InGaN/GaN Quantum Wells. *Appl. Phys. Express* **2012**, *5* (1), 014101.
(36) Koester, R.; Hwang, J. S.; Salomon, D.; Chen, X.; Bougerol, C.; Barnes, J. P.; Dang, D. L. S.; Rigutti, L.; Bugallo, A. L.; Jacopin, G.; Tchernycheva, M. M-plane Core−shell InGaN/GaN Multiple-Quantum-Wells on GaN Wires for Electroluminescent Devices. *Nano Lett.* **2011**, *11* (11), 4839−4845.
(37) Lai, K. Y.; Paskova, T.; Wheeler, V. D.; Chung, T. Y.; Grenko, J. A.; Johnson, M. A. L.; Udwary, K.; Preble, E. A.; Evans, K. R. Indium Incorporation in InGaN/GaN Quantum Wells Grown on m-Plane GaN Substrate and c-Plane Sapphire. *Phys. Status Solidi A* **2012**, *209*, 559−564.
(38) Messanvi, A.; Zhang, H.; Neplokh, V.; Julien, F. H.; Bayle, F.; Foldyna, M.; Bougerol, C.; Gautier, E.; Babichev, A.; Durand, C.; Eymery, J.; Tchernycheva, M. Investigation of Photovoltaic Properties of Single Core-Shell GaN/InGaN Wires. *ACS Appl. Mater. Interfaces* **2015**, *7* (39), 21898−21906.
(39) Sydoruk, V. A.; Xiang, D.; Vitusevich, S. A.; Petrychuk, M. V.; Vladyka, A.; Zhang, Y.; Offenhäusser, A.; Kochelap, V. A.; Belyaev, A. E.; Mayer, D. Noise and Transport Characterization of Single Molecular Break Junctions with Individual Molecule. *J. Appl. Phys.* **2012**, *112* (1), 014908.
(40) Xiang, D.; Pyatkov, F.; Schröper, F.; Offenhäusser, A.; Zhang, Y.; Mayer, D. Molecular Junctions Bridged by Metal Ion Complexes. *Chem. - Eur. J.* **2011**, *17* (47), 13166−13169.
(41) Muller, C. J.; Van Ruitenbeek, J. M.; De Jongh, L. J. Conductance and Supercurrent Discontinuities in Atomic-Scale Metallic Constrictions of Variable Width. *Phys. Rev. Lett.* **1992**, *69* (1), 140.
(42) Reed, M. A.; Zhou, C.; Muller, C. J.; Burgin, T. P.; Tour, J. M. Conductance of a Molecular Junction. *Science* **1997**, *278* (5336), 252−254.
(43) Lörtscher, E.; Ciszek, J. W.; Tour, J.; Riel, H. Reversible and Controllable Switching of a Single-Molecule Junction. *Small* **2006**, *2* (8−9), 973−977.
(44) Nadarajah, A.; Word, R. C.; Meiss, J.; Könenkamp, R. Flexible Inorganic Nanowire Light-Emitting Diode. *Nano Lett.* **2008**, *8* (2), 534−537.
(45) Weisse, J. M.; Lee, C. H.; Kim, D. R.; Zheng, X. Fabrication of Flexible and Vertical Silicon Nanowire Electronics. *Nano Lett.* **2012**, *12* (6), 3339−3343.
(46) Lee, J. Y.; Connor, S. T.; Cui, Y.; Peumans, P. Solution-processed Metal Nanowire Mesh Transparent Electrodes. *Nano Lett.* **2008**, *8* (2), 689−692.
(47) Lee, M. S.; Lee, K.; Kim, S. Y.; Lee, H.; Park, J.; Choi, K. H.; Kim, H. K.; Kim, D.-G.; Lee, D.-Y.; Nam, S. W.; Park, J. U. High-performance, Transparent, and Stretchable Electrodes using Gra-

DOI: 10.1021/acsami.6b06414
ACS Appl. Mater. Interfaces 2016, 8, 26198−26206

phene−Metal Nanowire Hybrid Structures. *Nano Lett.* **2013**, *13* (6), 2814−2821.
(48) Lavenus, P.; Messanvi, A.; Rigutti, L.; Bugallo, A. D. L.; Zhang, H.; Bayle, F.; Julien, F. H.; Eymery, J.; Durand, C.; Tchernycheva, M. Experimental and Theoretical Analysis of Transport Properties of Core−Shell Wire Light Emitting Diodes Probed by Electron Beam Induced Current Microscopy. *Nanotechnology* **2014**, *25* (25), 255201.
(49) de Luna Bugallo, A.; Tchernycheva, M.; Jacopin, G.; Rigutti, L.; Julien, F. H.; Chou, S. T.; Lin, Y.-T.; Tseng, P.-H.; Tu, L. W. Visible-blind Photodetector based on p−i−n Junction GaN Nanowire Ensembles. *Nanotechnology* **2010**, *21* (31), 315201.
(50) Monroy, E.; Munoz, E.; Sánchez, F. J.; Calle, F.; Calleja, E.; Beaumont, B.; Gibart, P.; Muñoz, J. A.; Cussó, F. High-performance GaN pn Junction Photodetectors for Solar Ultraviolet Applications. *Semicond. Sci. Technol.* **1998**, *13* (9), 1042.
(51) Krogstrup, P.; Jørgensen, H. I.; Heiss, M.; Demichel, O.; Holm, J. V.; Aagesen, M.; Nygard, J.; i Morral, A. F. Single-nanowire Solar Cells beyond the Shockley-Queisser Limit. *Nat. Photonics* **2013**, *7* (4), 306−310.
(52) Cavassilas, N.; Michelini, F.; Bescond, M. Modeling of Nanoscale Solar Cells: The Green's Function Formalism. *J. Renewable Sustainable Energy* **2014**, *6* (1), 011203.
(53) Cavassilas, N.; Gelly, C.; Michelini, F.; Bescond, M. *Theoretical Investigation of The Carrier Escape in InGaN Quantum Well Solar Cells.* In *IEEE Photovoltaic Spec. Conf., 42nd*, New Orleans, LA, USA, June 14−19, 2015; pp 1−3.

DOI: 10.1021/acsami.6b06414
ACS Appl. Mater. Interfaces 2016, 8, 26198−26206